Deciphering non-Gaussianity of diffusion based on the evolution of diffusivity

Haolan Xu,[1,3] Xu Zheng,[2,*] and Xinghua Shi[1,3,†]

[1]*Laboratory of Theoretical and Computational Nanoscience, National Center for Nanoscience and Technology, Chinese Academy of Sciences, Beijing 100190, China*

[2]*State Key Laboratory of Nonlinear Mechanics, Beijing Key Laboratory of Engineered Construction and Mechanobiology, Institute of Mechanics, Chinese Academy of Sciences, Beijing 100190, China*

[3]*University of Chinese Academy of Sciences, No. 19A Yuquan Road, Beijing 100049, China*

(Received 6 July 2023; revised 8 October 2023; accepted 12 March 2024; published 3 April 2024)

Non-Gaussian diffusion of nanoparticles in complex media disrupts Einstein's picture of Brownian motion, and non-Gaussianity is thought to be closely related to diffusing diffusivity generated by spatiotemporal heterogeneities. However, the correlation between non-Gaussianity and the dynamics of heterogeneous environments in anomalous diffusion remains uncertain. Inspired by a recent study by Alexandre *et al.* [Phys. Rev. Lett. **130**, 077101 (2023)], we demonstrate that non-Gaussianity can be deciphered through the spatiotemporal evolution of heterogeneity-dependent diffusivity distribution. Using diffusion experiments in a linear temperature field and Brownian dynamics simulations, we found that short-time non-Gaussianity can be predicted based on the boundary ratio of the diffusivity distribution; the long-time non-Gaussianity either approaches an asymptotic value of -2 or scales with $1/t$, depending on the dominance of particle migration. The temporal variation of non-Gaussianity is determined by an effective Péclet number, which represents a competition between the varying rate of diffusivity and the diffusivity of diffusivity and reveals whether the tail distribution expands or contracts. The tail is more Gaussian than exponential over long times, with exceptions significantly dependent on the diffusivity distribution. Our findings provide a versatile framework for understanding non-Gaussian diffusion in probability space, and shed light on establishing a diffusion spectrum in cells and characterizing nanomedicine transport in biological microenvironment using non-Gaussian statistics.

DOI: 10.1103/PhysRevResearch.6.023014

I. INTRODUCTION

The diffusion of microscopic particles is a key transport mechanism in various fields, including colloidal transport, biophysics, polymer science, and composite materials. In simple fluids, diffusion is described well by the theory of Brownian motion, which predicts two fundamental features [1]: the linear variation of the mean-squared displacement (MSD) and the Gaussian displacement probability distribution (DPD). However, in complex media with heterogeneities, the Fickianity and Gaussianity assumptions are sometimes invalid [2–13]. Examples of such anomalous diffusion of nanoparticles have been reported in living cells [3–6], polymer networks [7–10], active gels [11,12], and colloidal glasses [13].

In contrast to Gaussian behavior, non-Gaussianity indicates the presence of more complex dynamics related to extreme events or significant outliers in critical phenomena, phase transitions, and other emergent behaviors [3–18]. Notable examples include Fickian-yet-non-Gaussian diffusion (FnGD) found in actin networks and glassy materials [14,15]. The non-Gaussianity of diffusion in such complex media reflects structural or dynamical heterogeneity, serving as a crucial parameter for identifying anomalous mechanisms, characterizing rare events, and establishing statistical inferences [16–18]. Several theoretical models based on diffusing diffusivity (DifD) have been proposed to characterize FnGD [16–22]. These models build a primary framework to show the prevalence of non-Gaussianity and illustrate the tail that is commonly assumed exponential. However, the physical interpretation of non-Gaussianity in anomalous diffusion and its indication of underlying dynamics are unclear.

Given that the heterogeneity of a complex environment induces non-Gaussianity in diffusion, a central inquiry emerges: How can we comprehend the correlation between variations in non-Gaussianity and the degree of heterogeneity? The diffusivity distribution and its variation can be applied to map the structural or dynamical heterogeneity of a complex environment based on the DifD model, because they contain physical properties of the heterogeneous environment, such as viscosity, permeability, or energy barriers. The difficulty of quantifying the evolution of diffusivity, particularly in biological environments [22], makes the DifD model phenomenological and raises doubts regarding its validity. To

*zhengxu@lnm.imech.ac.cn
†shixh@nanoctr.cn

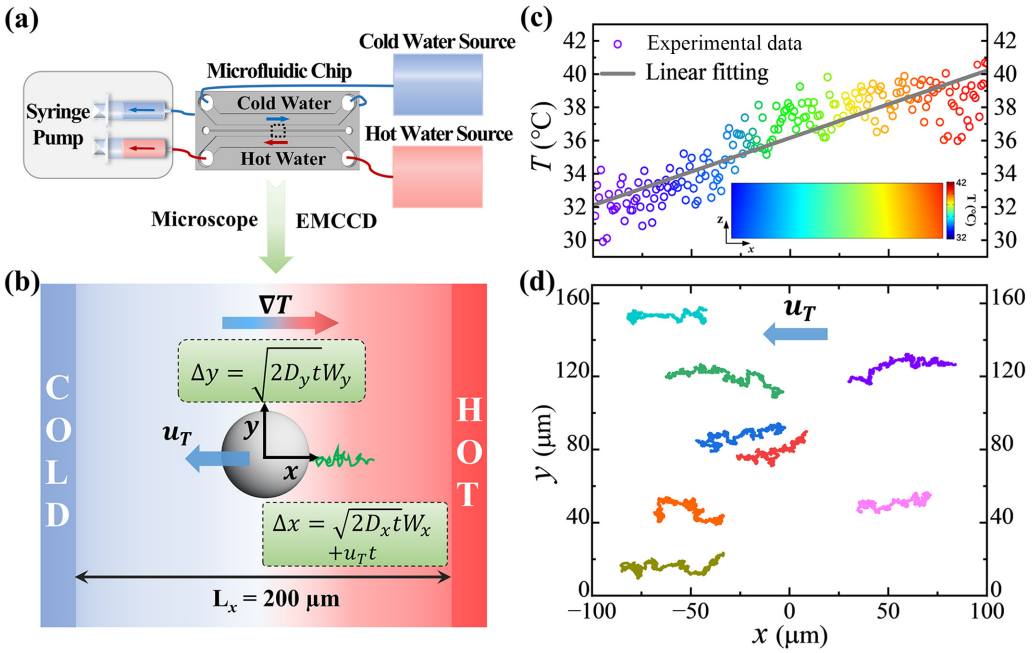

FIG. 1. (a) Experimental setup. A constant temperature gradient was created in the central microchannel of a microfluidic chip. (b) In the x axis (spanwise of microchannel), a particle moves toward the cold side along the temperature gradient, and its displacement is determined by thermophoresis and diffusion: $\Delta x(t) = \sqrt{2D_x t}W_x + u_T t$. In the y axis (streamwise of microchannel), the motion is diffusive with DifD: $\Delta y(t) = \sqrt{2D_y t}W_y$. (c) Experimental temperature distribution in the x axis when $\nabla T = 4.1 \times 10^4$ K/m. Inset: The simulation result of the uniform temperature field (Supplemental Material [26], Sec. S1); z axis is the height direction. (d) Representative trajectories of 1000 nm particles moving toward the cold side (left).

address this problem, among many recent efforts [23–25], an inspiring approach that drew an analogy with Taylor dispersion was proposed to mathematically link non-Gaussianity and heterogeneity [25]. Nonetheless, controversies regarding variations in non-Gaussianity and tail distribution remain unresolved.

In this study, we demonstrate that the thermophoretic colloidal response of collective nanoparticles to a temperature gradient can be used to model and explain non-Gaussian behavior in a heterogeneous field. We used thermophoresis of nanoparticles (NPs, diameters $d = 500$ and 1000 nm) in a microfluidic chip (Fig. 1(a), and Supplemental Material [26], Fig. S1(a)) [27] with a controlled temperature field to construct DifD of underlying probability space. By considering the heterogeneous field as a spatiotemporal evolution of diffusivity, we aimed to elucidate the correlation between non-Gaussianity and the DifD distribution $p(D)$ from the NPs' diffusion. As the NPs move along the constant temperature gradient (x axis) to the cold side with a constant thermophoretic speed u_T originating from interfacial flow of the NP surface [Fig. 1(b)], their diffusion perpendicular to the temperature gradient (y axis) experiences DifD determined by the temperature gradient, providing better controllability and quantifiability than that reported in recent studies [23–25,28]. Consequently, we can predict the short-time non-Gaussianity by the type and range of the DifD distribution, and show two long-time destinations depending on the presence of external field-driven migration. We found that the temporal variation of non-Gaussianity is determined by an effective Péclet number, which identifies the competition between the varying rate of diffusivity and the diffusivity of diffusivity. Unlike the majority perspective assuming an exponential tail, we will show why a Gaussian distribution is more suitable.

II. RESULTS AND DISCUSSION

A. Establishment of diffusing diffusivity using a thermophoretic microfluidic chip

We construct a microfluidic chip, same as our previous study [27], to establish stable and uniform temperature gradients. The microfluidic chip (Fig. 1(a), and Supplemental Material [26], Fig. S1(a)), which is made of stainless steel, builds a constant temperature gradient in the central microchannel (width = 200 μm, depth = 50 μm) through counterflow heat exchange between hot and cold water in two side channels (width = 2 mm, depth = 2 mm, length = 28 mm), ensuring a more uniform temperature gradient along the transverse direction (x axis) of the microchannel. All channels were sealed using an optical adhesive film (MicroAmp). By adjusting the flow rates of cold and hot water in both side channels via a dual-channel syringe pump (Longer Pump LSP02-1B), we achieved stable temperature gradients of $\nabla T = 4.1 \times 10^4$ and 6.6×10^4 K/m, corresponding to temperature differences of 8.1 and 13.2 K, respectively, in the central microchannel of the microfluidic chip [Figs. 1(a) and 1(c); see details in Appendix A]. In our experiments, the particles exhibit thermophoretic migration toward the cold side, and the thermophoretic mobility D_T was measured to be approximately $D_T = 10.0\,\mu\text{m}^2/(\text{s K})$ [27]. According to the thermophoretic velocity, $u_T = -D_T \nabla T$, $u_T = -0.40$ and -0.66 μm/s were obtained for the two respective temperature gradients.

Experimental observations were conducted using an inverted fluorescence microscope (Olympus, IX 71) fitted with a 40x/0.7 objective. Image acquisition was performed with an Electron-Multiplying CCD (EMCCD) camera (Andor iXon, 897) capturing consecutive frames at 20 frames per second (fps), corresponding to a time interval of 50 ms. The exposure time was set to 5 ms, and the image field of view was 512×512 pixels (approximately 200×200 μm), with each pixel representing approximately 390 nm and providing a spatial resolution of ~ 80 nm. At the beginning of each experiment, particles located at $x \in [-80, 90]$ μm were chosen for tracking lasting up to $\Delta t = 20$ s (see details in Appendix A). The observation plane was set at $z = 15$ μm using a piezo transducer (Physik Instrumente) mounted beneath the microscope objective, to avoid wall-induced hydrodynamic drag, as the relative distance $2z/d$ was large.

Figure 1(b) displays a schematic diagram of particle motion under the temperature gradient, and Fig. 1(d) shows the representative trajectories of NPs under $\nabla T = 4.1 \times 10^4$ K/m. As the particles move parallel to the constant temperature gradient toward the cold side at a constant thermophoretic velocity u_T, their temperature and viscosity experiences vary continuously along the x axis. Consequently, the NPs' displacement in the x axis is given by $\Delta x(t) = \sqrt{2D_x t}W_x + u_T t + t\partial D_x/\partial x \approx \sqrt{2D_x t}W_x + u_T t$, where W_x denotes an independent stochastic process with a mean of zero and standard deviation of 1, $D_x(T)$ is the local diffusivity depending on the temperature $T(x)$, and $\partial D_x/\partial x$ can be neglected as it is less than 1 nm/s. In the y axis, the displacement follows $\Delta y(t) = \sqrt{2D_y t}W_y$, which is determined by the DifD $D_y(t)$ varying with the NPs' thermophoretic migration along the temperature gradient in the x axis.

Our experimental design simplifies complexity by setting a controllable diffusing diffusivity and decoupling the diffusing diffusivity in the x axis from the diffusion in the y axis. Thanks to the controlled DifD, our system can effectively connect non-Gaussianity and the DifD, and monitor their temporal changes with ease. Our approach modeling the DifD based on such a linear temperature field can offer valuable insight into non-Gaussianity arising from heterogeneity with gradual variation. Besides, our approach can also approximate the heterogeneity with greater variation when the diffusion range is short.

B. Non-Gaussian behavior in experiments

The MSDs of 1000 nm particles under two temperature gradients are shown in Fig. 2(a), which is calculated by $\langle \Delta r^2(t) \rangle = \langle [r(t_0 + t) - r(t_0)]^2 \rangle$. Here, r represents x or y, and $\langle \cdots \rangle$ denotes the ensemble average. At short times, $t \approx 0.1$ s, all MSDs display a linear tendency, as Brownian diffusion is dominant. When $t > 2D_x/u_T^2 \sim 2$ s, the x-MSD $\langle \Delta x^2(t) \rangle$ gradually deviates from this linear due to the directional thermophoretic motion with a speed u_T, manifesting a superdiffusive behavior with a slope near 2. In contrast, the y-MSD $\langle \Delta y^2(t) \rangle$ approximates a Fickian behavior.

We then focus on the non-Gaussian behavior of this system. Recent studies have revealed that particle's diffusion might exhibit fat tails, even when the MSD appears linear [14,15]. The normalized DPDs of $\Delta y/\sigma$ at $t = 0.05$ s

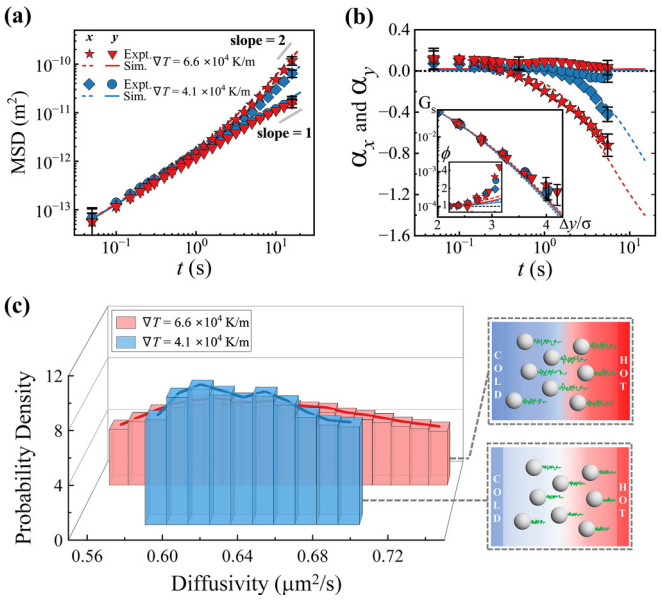

FIG. 2. Experimental (symbols) and simulation (curves) results of (a) MSD and (b) α for 1000 nm particles under $\nabla T = 6.6 \times 10^4$ and 4.1×10^4 K/m, respectively. The subscripts x and y represent the x direction and the y direction, respectively. The inset of (b) shows the normalized DPDs at $t = 0.05$ s; the tail ratio ϕ indicates the non-Gaussian fat tail of DPD when $\Delta y/\sigma > 3$. (The error bars here are determined based on uncertainties explained in the Supplemental Material [26], Sec. S1) (c) The diffusivity distributions $p(D)$ for different temperature gradients during $\Delta t = 20$ s.

were compared with the standard Gaussian distribution $G_s = \frac{1}{\sqrt{2\pi}}\exp[-(\Delta r/\sigma)^2/2]$ [Fig. 2(b)], where σ is the standard deviation of corresponding displacements. To quantify the amplification of the tailed DPD compared to the standard Gaussian distribution when $\Delta y/\sigma > 3$, we introduce the tail ratio ϕ, shown in the inset of Fig. 2(b). The maximum ratio ϕ was larger than 2, indicating a non-negligible non-Gaussian tail beyond the error bars, even though the motion in the y direction was purely diffusive. The non-Gaussian parameter $\alpha(t) = (\langle \Delta r^4(t) \rangle / \langle \Delta r^2(t) \rangle^2) - 3$ [25] is introduced to quantitatively assess the above non-Gaussian behavior [Fig. 2(b)]. For a Gaussian DPD, $\alpha = 0$, whereas positive and negative α values signify fat-tail leptokurtic and platykurtic distributions, respectively. In general, a greater temperature gradient ($\nabla T = 6.6 \times 10^4$ K/m) results in a larger non-Gaussian parameter α_y and a more pronounced fat tail at short times. With the uncertainty of α being less than ± 0.09 (Supplemental Material [26], Sec. S1), the experimental data of α_y suggest a slow decay from a positive $\alpha_y \approx 0.12$ when $t < 0.1$ s to $\alpha_y \approx 0$ when $t \approx 1$ s. When $t > 1$ s, α_y is still considered to be zero based on the error bars, which will be further confirmed by numerical simulations. In contrast, in the axis along the temperature gradient, α_x starts from a small positive value, similar to α_y, but decays more rapidly to a negative value when $t > 1$ s. Experiments using 500 nm NPs show similar results of MSD and DPD (Supplemental Material [26], Fig. S4).

Apart from the DPD, we provide the experimental results of the diffusivity distribution in Fig. 2(c). The effect of the

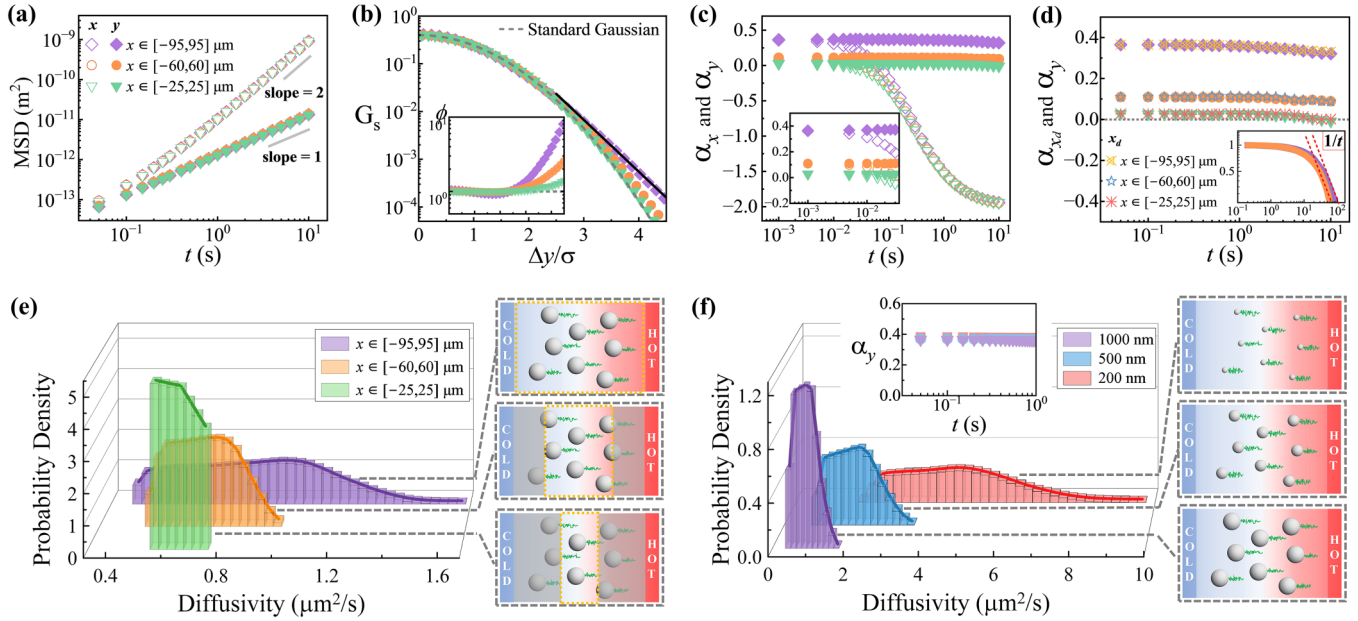

FIG. 3. (a)–(d) Simulation results for 1000 nm particles when $\nabla T = 3 \times 10^5$ K/m. The subscripts x, y, and x_d represent the x direction, the y direction, and the diffusive part in the x direction, respectively. The diffusivity distributions were controlled by setting different ranges of x. (a) MSDs. (b) DPDs at $t = 0.05$ s; inset is tail ratio ϕ. The solid line represents an exponential fit of $G_s \sim \exp[-\Delta y/(\sqrt{2D_y t})]$. (c) The variations in α_x and α_y. Inset: same initial values $\alpha_y = \alpha_x$ when $t \to 0$. The symbols of α_x and α_y are marked based on the legend in (a). (d) The variations in α_{xd} and α_y. Inset: Long-time scaling $1/t$ of normalized α_y. (e) The diffusivity distributions $p(D)$ for the three cases in (a). (f) The diffusivity distributions $p(D)$ for particles of different diameters. Temperature gradient: $\nabla T = 3 \times 10^5$ K/m, setting ranges of x position: $x \in [-95,\ 95]$ μm, duration $\Delta t = 15$ s.

diffusivity distribution on non-Gaussianity has not yet received sufficient attention, despite the variation of the distribution being crucial within the theoretical framework of diffusing diffusivity [16,17]. The sampled diffusivity distributions $p(D)$ of $\nabla T = 4.1 \times 10^4$ and $\nabla T = 6.6 \times 10^4$ K/m are respectively plotted in Fig. 2(c). The diffusivity distributions are nearly uniform as the particles were randomly sampled in the experiments. One can easily observe that a greater temperature gradient ($\nabla T = 6.6 \times 10^4$ K/m) not only results in a larger non-Gaussian parameter α_y, but also in a wider diffusivity distribution $p(D)$. This indicates that the non-Gaussian parameter α_y and the diffusivity distribution $p(D)$ originate from the same underlying diffusive dynamics and should have a quantitative correlation. This correlation will be further analyzed based on simulation results.

C. Brownian dynamics simulations: Unraveling the impact of spatiotemporal variation diffusivity on non-Gaussianity

To tackle the issue of limited long-time statistics in the experiments, we used Brownian dynamics simulations to complement the long-time evolution of non-Gaussianity (see details in Appendix B). By assigning the same thermophoretic speed and uniform diffusivity distribution along the x axis as the experiments, the simulation results [depicted by dashed and solid curves in Figs. 2(a) and 2(b)] closely match the experimental data. The long-time tendency of $\alpha_x(t)$ from the simulation collapses onto the extension of the experimental data when $t \sim 5$ s. Next, primarily based on the simulation results, we explore the effect of the spatiotemporal variation of DifD on non-Gaussianity. The initial distribution of D_r and its varying rate $\partial\langle D_r\rangle/\partial t \sim (\partial\langle D_r\rangle/\partial T)\nabla T u_T$ are controlled (Supplemental Material [26], Sec. S2), and the diffusivity of diffusivity, defined as $\partial\langle D_r^2\rangle/\partial t$, and the varying range of D_r are monitored.

We first test the non-Gaussianity at $\nabla T = 3 \times 10^5$ K/m, with a particle diameter $d = 1000$ nm. After subjecting the particles to thermophoresis with $u_T = -3.0$ μm/s for $\Delta t = 15$ s, the diffusivity distributions when ensemble statistics was conducted were regulated by approximately setting the ranges of x positions to $[-95, 95]$ μm, $[-60, 60]$ μm, and $[-25, 25]$ μm, respectively, from the initial positions $x \in [-50, 95]$ μm, $[-15, 60]$ μm, and $[20,25]$ μm (Supplemental Material [26], Sec. S2). A broader x range indicates a wider diffusivity distribution. In addition to the typical MSDs [Fig. 3(a)] and DPDs [Fig. 3(b)], similar to the experimental tendency, the variations in the non-Gaussian parameters in both directions are shown in Figs. 3(c) and 3(d). The short-time $\alpha_y(t)$ (solid symbols) starts from approximate constant values of 0.37, 0.11, and 0.03, respectively, following a gradual decay at $t > 2D_y/u_T^2 \sim 0.1$ s. The diffusivity distributions of the three cases are shown in Fig. 3(e). Notably, for a wider diffusivity distribution, the value of $\alpha_y(t)$ is larger and the tail is broader, which is in accordance with experimental observation in Figs. 2(b) and 2(c). Interestingly, the non-Gaussianity shown by dark-green symbols is similar to the experimental result with $\nabla T = 6.6 \times 10^4$ K/m [Fig. 2(b)]. This can be attributed to their analogous diffusivity ranges, approximately $0.55 - 0.74$ μm^2/s for the experiment with $\nabla T = 6.6 \times 10^4$ K/m, and $0.54 - 0.77$ μm^2/s for the Brownian dynamics simulation (dark-green symbols) with $\nabla T = 3 \times 10^5$ K/m, despite the differences in temperature gradients ∇T. When keeping

other conditions constant and changing particle diameters to $d = 200$ and 500 nm, almost identical values of short-time $\alpha_y \approx 0.38$ and 0.37 were obtained [Fig. 3(f); more details can be found in Appendix C, Fig. 9]. The size-independent result is counterintuitive, as particles with different diameters experience distinct diffusivity distributions as well. The above results imply that, rather than the absolute values of the diffusivity, non-Gaussianity may be influenced by the relative ratio of lower and upper boundaries of the diffusivity distribution, as will be proved theoretically later. In addition, the value of $\alpha_{xd}(t)$ [Fig. 3(d)], based on $\Delta x_d = \Delta x - u_T t$, is always almost the same as $\alpha_y(t)$. The value of $\alpha_x(t)$ [empty symbols in Fig. 3(c)] rapidly turns negative and reaches -2 at $t \sim 10$ s, despite sharing the same beginning as $\alpha_y(t)$.

D. Prediction of non-Gaussianity on a short-time scale

The above results demonstrate the significant influence of diffusivity distribution on non-Gaussianity and fat-tailed DPD. Recalling a recent study suggesting an analogy of DifD motion with Taylor dispersion [25], we find that the asymptotic features of non-Gaussianity can be accurately predicted only if the distribution of D_r is known. The mathematical derivation by Alexandre *et al.* [25] gives the fourth cumulant as $\langle \Delta r^4 \rangle - 3\langle \Delta r^2 \rangle^2 = 12\langle [\int_0^t \mathrm{d}s(D_r - \langle D_r \rangle)]^2 \rangle$. When $t \to 0$, the non-Gaussian parameter can be approximately calculated by dividing the variance $\mathrm{Var}(D_r)$ over the square of expectation $\langle D_r \rangle^2$ (see Appendix D for the full derivation):

$$\alpha_r(t \to 0) = 3\left(\left\langle D_r^2 \right\rangle - \langle D_r \rangle^2\right)/\langle D_r \rangle^2 = 3\mathrm{Var}(D_r)/\langle D_r \rangle^2. \tag{1}$$

Equation (1) establishes a correlation between $\alpha_r(t \to 0)$ and the diffusivity distribution $p(D_r)$ in a probability space, which explains the same initial values $\alpha_y = \alpha_x = \alpha_{xd}$ in Figs. 3(c) and 3(d) because they share the same diffusivity. This relation could be applied to various systems with structural or dynamical heterogeneities by mapping the heterogeneity onto DifD.

Surprisingly, from Eq. (1) we find that $\alpha_y(t \to 0)$ can be predicted solely based on the range ratio $\beta(\Delta t) = D_{\min}/D_{\max}$. The dependence of $\alpha_y(t \to 0)$ on β indicates that $\alpha_y(t \to 0)$ should be independent of particle diameter d, considering that $D_{\min}$ and $D_{\max}$ are both inversely proportional to d. This deduction provides an explanation for the size-independent result in Fig. 3(f). In the following, we will show in detail the relation between the short-time non-Gaussianity $\alpha_y(t \to 0)$ and the range ratio β determined by the boundaries of the diffusivity distribution.

We first take a uniform distribution of $D_y \in [D_{\min}, D_{\max}]$ as an example, which approximates our experimental sampling. As the variance of this uniform distribution is $\mathrm{Var}(D_r) = (D_{\max} - D_{\min})^2/12$ and the square of expectation $\langle D_r \rangle^2 = (D_{\max} + D_{\min})^2/4$, according to Eq. (1), the short-time non-Gaussian parameter becomes (see Appendix D for the full derivation)

$$\alpha_y(t \to 0) = \frac{3\mathrm{Var}(D_y)}{\langle D_y \rangle^2} = \left(\frac{D_{\max} - D_{\min}}{D_{\max} + D_{\min}}\right)^2 = \left(\frac{1-\beta}{1+\beta}\right)^2. \tag{2}$$

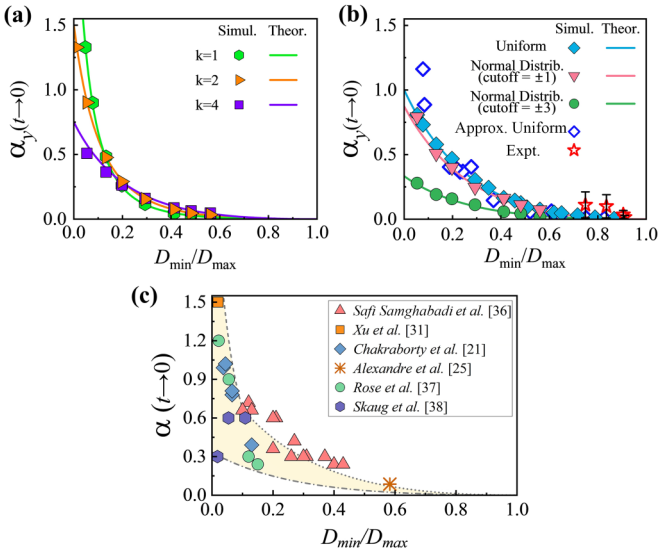

FIG. 4. (a), (b) Determination of $\alpha_y(t \to 0)$ based on $D_{\min}/D_{\max}$ for (a) gamma distribution, and (b) uniform distribution and truncated normal distribution. (c) A comparison of our prediction with existing non-Gaussian results from the literature based on the plot of $\alpha(t \to 0)$ vs $\beta = D_{\min}/D_{\max}$. The light-yellow belt schematically displays the region of our theoretical prediction, with lower boundary from normal distribution of diffusivity [dash-dotted curve, also the dark-green curve from (b)] and upper boundary consisting of uniform distribution of diffusivity [dotted curve, also the blue curve from (b)] and gamma distribution [$k = 1$, dashed curve, also the light-green curve from (a)].

We then consider gamma distribution $p(D_y) = D_y^{k-1}\exp(-D_y)/\Gamma(k)$ truncated at $D_y \in [D_{\min}, D_{\max}]$, which has been found to be a proper description of the diffusivity distribution in many complex biological media [4,29–35]. By mapping it to a standard gamma distribution $p(z) = z^{k-1}\exp(-z)/\Gamma(k)$ truncated at $z \in [0, N] : (D_y - D_{\min})/(D_{\max} - D_{\min}) = z/N$, we obtain $\mathrm{Var}(D_y) = \mathrm{Var}(z)(D_{\max} - D_{\min})^2/N^2$ and $\langle D_y \rangle = \langle z \rangle (D_{\max} - D_{\min})/N + D_{\min}$. For large N such as $N = 10$, $\mathrm{Var}(z) \approx k$ and $\langle z \rangle \approx k$, $\alpha_y(t \to 0)$ of the gamma distribution is (see Appendix D for the full derivation)

$$\alpha_y(t \to 0) = 3k\left[\frac{1-\beta}{k(1-\beta) + N\beta}\right]^2. \tag{3}$$

Additionally, the expression of $\alpha_y(t \to 0)$ for normal distributions is derived as (see Appendix D for the full derivation):

$$\alpha_y(t0) = \frac{3}{N^2}\left(\frac{1-\beta}{1+\beta}\right)^2. \tag{4}$$

Note that by mapping to a standard normal distribution truncated at $z \in [-N, N]$, $\alpha_y(t \to 0) = \frac{3}{N^2}(\frac{1-\beta}{1+\beta})^2$ is valid only when the truncated range $N \geqslant 3$. The expression of $\alpha_y(t \to 0)$ when $N < 3$ is given in Appendix D, which predicts a larger non-Gaussianity owing to a stronger dispersion of D_y [shown by the pink curve in Fig. 4(b) for $N = 1$].

We perform Brownian dynamics simulation to verify the relation between $\alpha_y(t \to 0)$ and $\beta = D_{\min}/D_{\max}$ as outlined in Eqs. (2)–(4). In these simulations, we respectively assign uniform, gamma, and normal distributions to D_y and maintain

∇T and u_T unchanged. The simulation results for gamma distribution [Fig. 4(a)] with different shape parameters, $k = 1$, 2, and 4, are in good agreement with the prediction curve from Eq. (5). It is interesting to see that in Fig. 4(a) the curve of $\alpha_y(t \to 0)$ becomes smoother for larger shape parameter k. Similar good agreements are observed in Fig. 4(b) for uniform distribution, normal distributions truncated at $N = 1$, and $N = 3$, respectively. Our theoretical approach can be extended to other exponential or power-law distributions, and can be widely used to evaluate non-Gaussianity in complex scenarios.

The theoretical analysis above indicates that, for a given diffusivity distribution, the short-time non-Gaussianity $\alpha_y(t \to 0)$ is determined by the ratio $\beta = D_{\min}/D_{\max}$ and diminishes with the increasing β. This finding is in good agreement with our previous results that short-time non-Gaussianity can be enhanced by broader diffusivity distribution. It also elucidates the counterintuitive result in Fig. 3(f), as the values of β in the simulations using particles of different diameters are very similar. We also draw experimental data of $\alpha_y(t \to 0)$ [red stars in Fig. 4(b)] acquired from approximately uniform samples, which decrease with the increasing β. The experimental data are located near the theoretical curve of uniform distribution, with deviations falling within the error bars.

Furthermore, we gather experimental data of the short-time non-Gaussian parameter $\alpha(t \to 0)$ and diffusivity ratio β from recently published literature spanning diverse fields and compare them with our model [Fig. 4(c)]. Most previous results have not paid attention to the correlation of non-Gaussianity and diffusivity distribution; we can only find a few data that provided a clue for estimating β from the literature (Supplemental Material [26], Sec. S3). Given that the types of the diffusivity distributions are generally indeterminate, we improved comparability of the gathered data with our theoretical predictions by representing our model's prediction range as a light-yellow band in Fig. 4(c). The lower boundary of this band is derived from normal distribution of diffusivity ($N = 3$, dash-dotted curve), and the upper boundary consists of uniform distribution (dotted curve) and gamma distribution ($k = 1$, dashed curve). Significantly, our model predictions demonstrate substantial agreement with the literature results, illustrating the validity of using our model to predict non-Gaussianity and correlate diffusivity distribution with underlying non-Gaussian dynamics. For instance, Safi Samghabadi *et al.* [36] [pink triangles in Fig. 4(c)] investigated the diffusion dynamics of semiflexible M13 bacteriophage within semidilute sodium polystyrenesulfonate solutions. The anisotropy of the bacteriophage induced varied degrees of interaction with polymers, resulting in the emergence of non-Gaussian dynamics. The study on the diffusion behavior of individual lipids within a membrane during the membrane actions of peptides [31,34] similarly emphasizes that stronger interactions lead to increased heterogeneity, consequently yielding higher non-Gaussian parameters [orange square in Fig. 4(c)]. These two biological context outcomes are observed to be located close to the upper edge of our prediction belt in Fig. 4(c). Expanding our comparison to other systems with diffusivity fluctuations or structural heterogeneity reveals the broad applicability of our model. This is supported by studies on colloidal systems, such as the examination of particle diffusion in structurally diverse micropillar matrices [21] [blue diamonds in Fig. 4(c)] and regions near surfaces [25] [brown asterisk in Fig. 4(c)]. Similarly, in polymer systems, our prediction aligns with the result of the diffusion of quantum dot and quantum rod in tetra-poly (ethylene glycol) (tetra-PEG) hydrogel before gelation [37] [green circles in Fig. 4(c)]. In porous media systems, non-Gaussian data of particle diffusion in porous polymer films [38] [purple hexagons in Fig. 4(c)] also fall within the prediction region.

It is worth mentioning that $\alpha_y(t \to 0)$ in our simulation only varies slightly with the duration Δt, as the change of $\beta(\Delta t)$ is tiny during the slow evolution of diffusivity distribution, which has been manifested by the short-time plateau of $\alpha_y(t)$ in Figs. 3(c) and 3(d). For relatively long duration like $\Delta t = 15$ s, the data of $\alpha_y(t \to 0)$ [empty blue diamonds in Fig. 4(b)] are close to the theoretical curve of uniform distribution when the diffusivity distribution is still approximately uniform. Nonetheless, with the increasing of Δt, the deviation will increase as well because the distribution departs from the initial uniform distribution, which has been displayed by the regions near the upper boundary of $p(D)$ in Figs. 3(e) and 3(f). Our results illustrate that non-Gaussianity in the same system can vary significantly depending on the sampling range of $p(D_r)$. In particular, ergodic sampling with a minimal value of β can exhibit a much larger non-Gaussianity than truncated sampling with a larger β, as illustrated in Figs. 4(a) and 4(b).

E. Prediction of non-Gaussianity on a long-time scale

We then consider the long-time limit of non-Gaussianity in Figs. 3(c) and 3(d). Although calculating the temporal evolution of $p(D_r)$ is complicated for various heterogeneities, previous work [25] has predicted that $\alpha_r(t)$ should decay with $1/t$ at long times. We indeed observed a $1/t$ decay to zero of α_y when $t \sim 100$ s [inset of Fig. 3(d)] in our simulation, when boundary confinement was absent. In realistic cases with confinement [24,25], $1/t$ decay was observed later when $t \sim 1000$ s. This long-time scaling $1/t$ is assumed to be an intrinsic feature owing to diffusivity dispersion, which is independent of boundary confinement.

Distinct from the positive non-Gaussianity, the most evident feature of $\alpha_x(t)$ is the long-time asymptotic value $\alpha_x(t \to \infty) = -2$ owing to the thermophoresis. Substituting thermophoretic term $\Delta x(t) = \sqrt{2D_x t}W_x + u_T t$ into the equation of the non-Gaussian parameter $\alpha_x(t) = (\langle \Delta x^4 \rangle - 3\langle \Delta x^2 \rangle^2)/\langle \Delta x^2 \rangle^2$, one obtains $\alpha_x(t) = (4\langle D_x^2 \rangle / u_T^4 t^2 - 12\langle D_x \rangle^2 / u_T^4 t^2 - 2)/(4\langle D_x^2 \rangle / u_T^4 t^2 + 4\langle D_x \rangle^2 / u_T^4 t^2 + 1)$. The long-time limit is $\alpha_x(t \to \infty) = -2$ if $\langle D_x^2 \rangle \ll u_T^4 t^2$. An intriguing inference is that the asymptotic value $\alpha_x(t \to \infty) = -2$ will appear for external field-driven migration with a large speed $u_T^4 t^2 \gg \langle D_x^2 \rangle$.

F. Temporal variation of non-Gaussianity governed by an effective Péclet number

Unlike the experiment which reported a rapid increase in non-Gaussianity at short times [24], our experimental and simulation results show a constantly decreasing $\alpha_y(t)$.

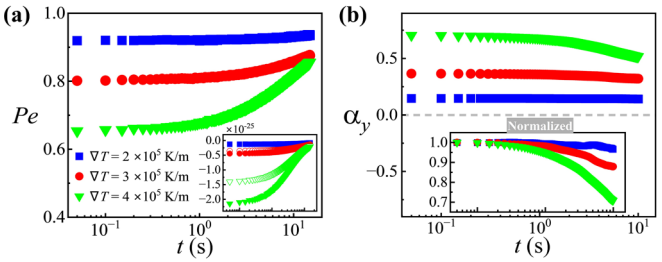

FIG. 5. (a) Temporal variation of Pe under different temperature gradients. Inset: $\frac{\partial\langle D_y^2\rangle}{\partial t}$ (solid symbols) and $\frac{\partial\langle D_y\rangle^2}{\partial t}$ (open symbols). (b) $\alpha_y(t)$ and corresponding curves normalized by the maximum values shown in inset.

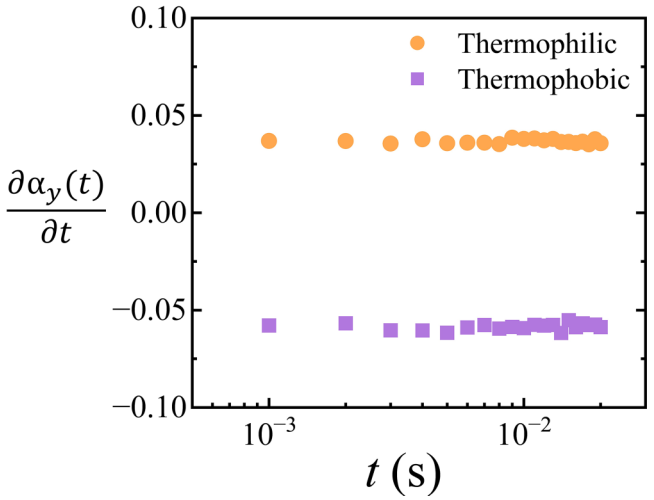

FIG. 6. Simulation result shows that the short-time temporal variation of $\frac{\partial\alpha_y(t)}{\partial t}$ can be changed from negative to positive by tuning the particle's thermophoresis from thermophobic (purple solid squares, indicating particles move to the cold side and $D_T > 0$) to thermophilic (orange solid circles, indicating particles move to the hot side and $D_T < 0$); temperature gradient is $\nabla T = 3\times10^5$ K/m.

Next, we discuss the tendency of $\alpha_y(t)$ by the derivative $\frac{\partial\alpha_y(t)}{\partial t} \sim \frac{1}{\langle D_y\rangle^2}(\frac{\partial\langle D_y^2\rangle}{\partial t} - 2\alpha_y\langle D_y\rangle\frac{\partial\langle D_y\rangle}{\partial t})$, which shows a competition between $\frac{\partial\langle D_y^2\rangle}{\partial t}$ and $\frac{\partial\langle D_y\rangle}{\partial t}$, referred to as the diffusivity of diffusivity and the varying rate of diffusivity, respectively. This competition defines an effective Péclet number $\mathrm{Pe} = (\langle D_y\rangle\frac{\partial\langle D_y\rangle}{\partial t})/\frac{\partial\langle D_y^2\rangle}{\partial t}$, which helps assess whether $\alpha_r(t)$ will increase or decrease with time. Here, $\langle D_y\rangle$, $\frac{\partial\langle D_y\rangle}{\partial t}$, and $\frac{\partial\langle D_y^2\rangle}{\partial t}$ can be seem as equivalent length, velocity, and diffusivity, respectively, in a space of D_y, in analogy to traditional Pe number in Taylor dispersion.

As the varying rate can be approximated as $\frac{\partial\langle D_y\rangle}{\partial t} \sim (\partial < D_y > /\partial T)\nabla T u_T \sim \nabla T^2 \sim u_T^2$, in Figs. 5(a) and 5(b) we adjust the temperature gradient ∇T to investigate its influence on the variations of Pe and α_y. Both the diffusivity of diffusivity $\frac{\partial\langle D_y^2\rangle}{\partial t}$ (solid symbols) and the varying rate $\frac{\partial\langle D_y\rangle^2}{\partial t}$ (open symbols) are negative [inset of Fig. 5(a)], whereas the domination of the diffusivity of diffusivity, i.e., $|\frac{\partial\langle D_y^2\rangle}{\partial t}| > |\frac{\partial\langle D_y\rangle^2}{\partial t}|$, results in $\mathrm{Pe} < 1$ and $\frac{\partial\alpha_y(t)}{\partial t} < 0$. A larger ∇T, indicating an increased in the degree of heterogeneity, leads to a larger $\alpha_y(t)$ and a smaller Pe number as the ratio $|\frac{\partial\langle D_y\rangle^2}{\partial t}|/|\frac{\partial\langle D_y^2\rangle}{\partial t}|$ decreases with increasing ∇T. The competition between $\frac{\partial\langle D_y^2\rangle}{\partial t}$ and $\frac{\partial\langle D_y\rangle}{\partial t}$ depicts the following two-stage variation: at short times, the leading contribution $\frac{\partial\langle D_y^2\rangle}{\partial t}$ is dominated by diffusion, resulting in slow variations of both Pe and $\alpha_y(t)$ and a smaller Pe number; at intermediate times when thermophoretic motion is dominant over diffusion, $\frac{\partial\langle D_y\rangle}{\partial t} \sim u_T$ becomes significant, causing a fast increase of Pe number and a fast decay of $\alpha_y(t)$.

Interestingly, the above analysis predicts a positive $\frac{\partial\alpha_y(t)}{\partial t}$ at short times if $\frac{\partial\langle D_y^2\rangle}{\partial t}$ and $\frac{\partial\langle D_y\rangle^2}{\partial t}$ turn positive while $|\frac{\partial\langle D_y^2\rangle}{\partial t}| > |\frac{\partial\langle D_y\rangle^2}{\partial t}|$ is maintained. As shown in Fig. 6, by changing the NP from thermophobic to thermophilic, we obtained positive $\frac{\partial\alpha_y(t)}{\partial t}$ in the simulation at short time, approximately at $t \sim 0.01$ s. Nonetheless, the increase in short-time non-Gaussianity in our simulation was much weaker than the rapid dynamics reported by Pastore *et al.* [24]. We speculate that the difference was due to a sudden dispersion of $\frac{\partial\langle D_r^2\rangle}{\partial t}$ produced by the optical-illumination speckle [24]. The different non-Gaussian behaviors between the present system with slow DifD and the systems with rapid dynamics, such as glassy materials [13], can serve to detect specific short-time mechanisms.

G. Evolution and generic form of fat-tailed DPD

After clarifying the correlation between non-Gaussianity and distribution $p(D)$, we further discuss how $p(D)$ determines fat-tailed DPD, which is the most prominent feature of FnGD. Whether the tail of the DPD is exponential remains controversial [8,15,25,39], although a good exponential fit is observed in Fig. 3(b). Mathematically, the DPD $G_s(\Delta y,\, t) = \int p(D_y)p(\Delta y|D_y)\mathrm{d}D_y$ following Bayes' theorem can be rewritten as $G_s(\Delta y,\, t) = \int_{D_{\min}}^{D_{\max}} \frac{p[D_y(x)]}{\sqrt{4\pi D_y(x)t}}\exp[-\frac{\Delta y^2}{4D_y(x)t}]\mathrm{d}D_y$. $D_y(T)$ is determined by the temperature field. This integral can be approximated as $G_s(\Delta y,\, t) \approx C\exp[-\frac{\Delta y^2}{4D_y(x^*)t}]$ based on the Laplace approximation for large Δy, where prefactor C depends on $p(D_y)$, and x^* is the position of maximum $D_y(x^*)$ (see Appendix D for the full derivation). This approximation could help clarify the controversy regarding the tail as the term $\exp[-\frac{\Delta y^2}{4D_y(x^*)t}]$ suggests a more Gaussian tail for large Δy, which contradicts many existing results of exponential tails [7,8,14,24,39].

As shown in the double-logarithmic plot of $\ln(G_s\sqrt{2\pi})$ vs $\Delta y/\sigma$ in Fig. 7, the slopes of gamma and normal distributions are approximately -2 (Gaussian) for the tail $\Delta y/\sigma > 3$. The function type of $p(D_y)$ can influence the result of the integral by the prefactor C in the Laplace approximation. For the uniform distribution of $p(D_y)$, the slope of the tail deviates from -2 when $\Delta y/\sigma > 3$ and becomes -1 near $\Delta y/\sigma = 6$. This is consistent with the prediction of an exponential tail if $\partial\ln[p(D_y)]/\partial D_y$ is constant, as reported by Wang *et al.* [15], using the steepest descent analysis for the integral $G_s \sim \int \exp(\ln[p(D_y)] - \frac{\Delta y^2}{4D_y t})/\sqrt{D_y}dD_y$. Although the Gaussian tail for the gamma distribution is distinct from the prediction in

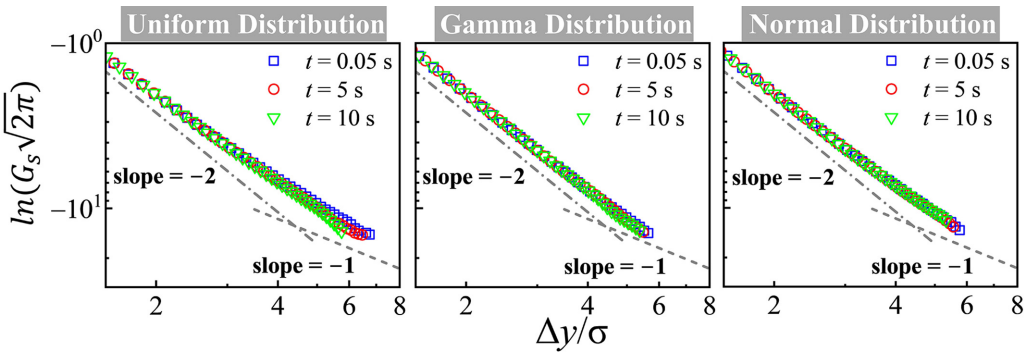

FIG. 7. $\ln(G_s\sqrt{2\pi})$ vs $\Delta y/\sigma$ for different distributions $p(D_y)$ at $t = 0.05 - 10$ s. The slope of -2 means G_s is Gaussian, whereas -1 means G_s is exponential.

Refs. [15,16], it is in accordance with Alexandre *et al.* [25], where a generic Gaussian tail was proposed. Additionally, a slight contraction of the tail turning more Gaussian with time is observed for uniform and gamma distributions as the Gaussian term $\exp[-\frac{\Delta y^2}{4D_y(x^*)t}]$ becomes more significant for large Δy. The transition from a short-time exponential-like tail to a long-time Gaussian-like tail could clarify the controversy that similar systems may display contradictory tail shapes. As an exception, diffusion in strongly confined media [8], where statistical data cannot reach a sufficiently large Δy, typically manifests an exponential tail.

H. Asymmetric fat-tailed DPD in the *x* direction

Along the x direction parallel to the temperature gradient, the thermophoretic motion of NPs can cause an asymmetric fat-tailed distribution, contrasting with the symmetric behavior found in the y direction. This biased distribution can be quantified by skewness, denoted as $S(\Delta t) = \langle[\Delta r(\Delta t) - \langle\Delta r(\Delta t)\rangle]^3\rangle/\langle[\Delta r(\Delta t) - \langle\Delta r(\Delta t)\rangle]^2\rangle^{3/2}$. Nonzero skewness indicates a departure from symmetrical fat-tail distribution. Given the expression for $\Delta x(t) = \sqrt{2D_x t}W_x + t\frac{\partial D_x}{\partial x} + u_T t$, and an approximated $\frac{\partial\langle D_x\rangle}{\partial t} \sim (\partial\langle D_x\rangle/\partial x)u_T$, the term $\partial\langle D_x\rangle/\partial x$ can lead to an asymmetric fat-tailed distribution over longer time, deviating from the symmetric behavior observed in the y direction. As shown in Fig. 8(a), the x skewness significantly increases over time with an increasing temperature gradient, while the y skewness remains constant at zero. Figure 8(b) shows the DPD under a temperature gradient $\nabla T = 4 \times 10^5$ K/m, where the fat-tailed distribution increasingly deviates from symmetry over time.

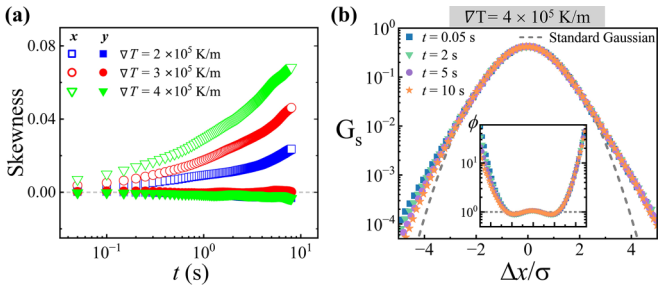

FIG. 8. (a) Skewness. (b) DPDs under a temperature gradient $\nabla T = 4 \times 10^5$ K/m, with the inset showing the tail ratio ϕ.

III. CONCLUSIONS

We used the thermophoretic colloidal response of collective nanoparticles to a temperature gradient to explain non-Gaussian behavior in a heterogeneous field. We investigated non-Gaussian diffusion of NPs in such thermophoretic system with a controlled DifD, and we successfully correlated non-Gaussianity with the spatiotemporal evolution of diffusivity distribution of the nanoparticles. Short-time non-Gaussianity was predicted based on the range ratio $\beta = D_{\min}/D_{\max}$ of diffusivity distribution $p(D)$, which is determined by the boundaries rather than the absolute value of $p(D)$. We demonstrated the predictive power using uniform, normal, and gamma distributions. The variation in non-Gaussianity at intermediate times was determined by the effective Pe number, which characterizes the competition between the varying rate of diffusivity and the diffusivity of diffusivity. This explains why the tail of the DPD usually contracts, unless it is influenced by sudden dynamics that enhance the diffusivity of diffusivity. The long-time decay of non-Gaussianity followed a $1/t$ scaling in a purely diffusive process, whereas in the presence of particle migration, the non-Gaussianity eventually reached -2. Furthermore, using Laplace's approximation of Bayes' theorem, we depicted that the tail was more Gaussian than exponential. We showed the transition from a short-time exponential-like tail to a long-time Gaussian-like tail to clarify the controversies in existing experiments. Notably, our theoretical model has been found in good agreement with results from the literature, illustrating a unique way to correlate diffusivity distribution with underlying non-Gaussian dynamics across different systems.

Although our approach models the DifD only based on a linear temperature field, it can offer valuable insight into non-Gaussianity arising from heterogeneity with gradual variation. Our results shed light on heterogeneity mapping in complex environments, for example, establishing the diffusion spectrum of a cell based on non-Gaussian statistics, and characterizing nanomedicine transport in a biological microenvironment [30,40–44]. The idea contains mapping heterogeneity-dependent diffusion diffusivity by non-Gaussian parameters and detecting a microscopic mechanism

based on the temporal variation of non-Gaussianity, echoing the recent result of Bayesian deep learning deciphering the physics encoded in diffusion data [45].

ACKNOWLEDGMENTS

This work was supported by the National Key R&D Program of China (Grants No. 2022YFA1203200 and No. 2022YFF0503504), the Strategic Priority Research Program of the Chinese Academy of Sciences (Grant No. XDB36000000), the Scientific Instrument Developing Project of the Chinese Academy of Sciences (Grant No. YJKYYQ20200019), the Natural Science Foundation of Beijing (Grants No. 2222085, No. 1202023, and No. 2194092), the National Natural Science Foundation of China (Grants No. 12072350, No. 11972351, No. 12102456, No. 11672079, No. 12072082, and No. 12125202). The authors thank the Hefei Advanced Computing Center for computational resources.

APPENDIX A: EXPERIMENTAL METHODS

1. Temperature gradient characterization

The temperature profiles in the microchannel were verified by a temperature-sensitive fluorescence, Rhodamine B (#83689, Sigma-Aldrich) [27,46]. In our experiments, when the flow rates of hot (80 °C) and cold (0 °C) water in the two side channels were set to $Q = 5$ ml/min, the measured temperature difference was approximately 8.1 K ($\nabla T = 4.1 \times 10^4$ K/m), in excellent agreement with simulation results using COMSOL (Fig. 1(c), and Supplemental Material [26], Sec. S1). Upon increasing the flow rates to $Q = 15$ ml/min, the temperature difference was approximately 13.2 K ($\nabla T = 6.6 \times 10^4$ K/m), which is the maximum stable temperature gradient that can be stably achieved in the current experimental system.

2. Particle tracking

The fluorescent polystyrene (PS) particles with diameters of $d = 500$ nm (F8812) and $d = 1.0\,\mu$m (F8819) were procured from Thermo Fisher Scientific Inc. The surface zeta potentials of the PS particles were measured to be approximately -32.8 mV for 500 nm particles, and -35.1 mV for 1.0 μm particles (Malvern Panalytical, Zetasizer Nano ZS). To facilitate particle tracking, the original particle suspensions were diluted with DI water (Milli-Q, 18.2 MΩ cm) to a concentration below 0.1 wt %. Particle tracking and trajectory analysis were performed using IMAGEJ along with a custom MATLAB algorithm. Initially, in each experiment, we selected particles uniformly within the range of $x \in [-80,\ 90]\,\mu$m for tracking. The tracking duration was set at 20 s (corresponding to 400 frames), and up to 50 000 particle displacements could be obtained for statistical calculation. Tracking was terminated if a particle approached the side wall too closely. In the case of $\nabla T = 6.6 \times 10^4$ K/m with a thermophoretic velocity $u_T = -0.66\,\mu$m/s, a particle beginning at $x = -80\,\mu$m would finally move to approximately $x = -93.2\,\mu$m during 20 s. Thus the particle positions were approximately $x \in [-95,\ 90]\,\mu$m, was defined as $D_{\min} \approx 0.557\,\mathrm{mm}^2/\mathrm{s}$ and $D_{\max} \approx 0.744\,\mathrm{mm}^2/\mathrm{s}$ [Fig. 2(c)], resulting in the range ratio $\beta = D_{\min}/D_{\max} = 0.749$ [Fig. 4(b)].

APPENDIX B: BROWNIAN DYNAMICS SIMULATION

We employed the finite-difference method in Brownian dynamics simulations. By utilizing Itô calculus, the overdamped Langevin equation can be expressed as

$$\mathrm{d}\boldsymbol{r} = \sqrt{2D_r}\int_0^t \mathrm{d}\boldsymbol{W}(t') = \sqrt{2D_r}\boldsymbol{W}(t). \tag{B1}$$

Here, $\boldsymbol{W}(t)$ is a random walk with diffusion coefficient D, known as the Wiener process, with a zero mean and standard variation of 1. As the NPs move along this constant gradient toward the cold side at a constant thermophoretic velocity u_T, they experience a continuous change in both temperature $T(x)$ and viscosity $\eta(x)$ dependent on their position. The local diffusion coefficient $D_y = D_x$, derived from the Stokes-Einstein equation, can be determined as $D_y = D_x = \frac{k_B T(x)}{\gamma(x)} = \frac{k_B T(x)}{3\pi\eta(x)d}$, where k_B is Boltzmann's constant. By defining the velocity $\boldsymbol{v}$ as the change in position $\Delta\boldsymbol{r}$ over time Δt and explicitly writing $\Delta\boldsymbol{r} = \boldsymbol{r}_{n+1} - \boldsymbol{r}_n$, the finite-difference equations is obtained as

$$\begin{aligned} x_{n+1} &= x_n + \sqrt{2D_x\Delta t_s}W_{x,n} + \Delta t\frac{\partial D_x}{\partial x} + u_T\Delta t_s, \\ y_{n+1} &= y_n + \sqrt{2D_y\Delta t_s}W_{y,n}. \end{aligned} \tag{B2}$$

For a given step $\Delta t_s = 10^{-4}$ s, these equations yield the sequence of $\{x_n,\ y_n\}$, representing the trajectory of the particle in the xy plane. The number of particles involved in each simulation $N_p = 5 \times 10^5 - 1 \times 10^6$. The simulation employed physical parameters identical to those used in the experiments. We utilized a high-performance computing environment on a supercomputer, optimizing computational efficiency and overall performance.

APPENDIX C: PARTICLE SIZE EFFECT

We compared the non-Gaussian diffusion behavior of NPs with different diameters under the same conditions. The simulation results for NP diameters of 200, 500, and 1000 nm under a temperature gradient $\nabla T = 3 \times 10^5$ K/m are shown in Fig. 9. It can be observed that the y-MSD curves are all approximately linear, although they shift upward as the NP's size decreases, as predicted by the Stokes-Einstein relation. The x-MSDs are primarily influenced by the thermophoretic motion with a speed u_T at long times, leading to an overlap of x-MSDs curves, demonstrating a superdiffusive behavior with a slope close to 2. The temporal transition from normal diffusion (slope = 1) to superdiffusion (slope = 2) is dependent on the NP's size, with $t \sim 2D_x/u_T^2$. Interestingly, the y-DPDs of all three NPs yield consistent results, regardless of the NP's size. The non-Gaussian parameter α_y exhibits nearly identical values, as the diffusivity range ratios β in simulations with particles of different diameters are very similar. In contrast, α_x values decay to negative values at different times, eventually reaching a plateau at approximately -2. Notably, the x skewness exhibits significant differences among the NPs of different diameters. As the diameter decreases, the x skewness experiences a substantial increase, which can be attributed to the contribution of $\partial\langle D_x\rangle/\partial x$ to its value.

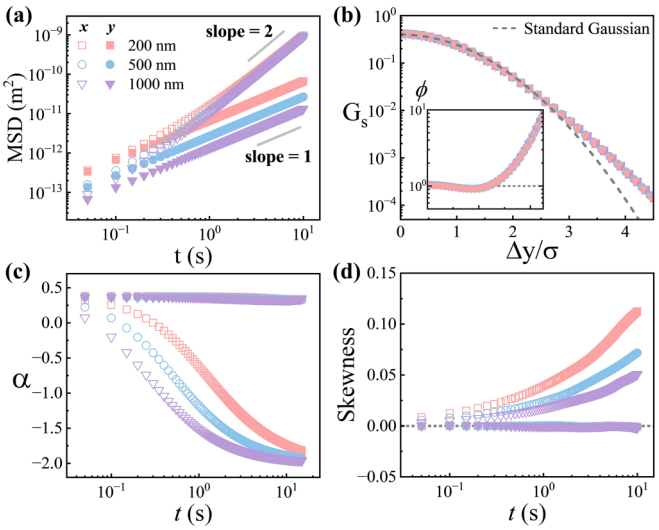

FIG. 9. Simulation results of 200, 500, and 1000 nm NPs under $\nabla T = 3 \times 10^5$ K/m. (a) MSDs. (b) DPDs at $t = 0.05$ s, with the inset showing the tail ratio ϕ. (c) Non-Gaussian parameter α. (d) Skewness.

APPENDIX D: MATHEMATICAL DERIVATION

1. Mathematical derivation for α

Alexandre *et al.* [25] utilized Wick's theorem to derive the expression for the fourth cumulant $\langle \Delta r^4 \rangle_c$, which is given by

$$\langle \Delta r^4 \rangle_c = \langle \Delta r^4 \rangle - 3\langle \Delta r^2 \rangle^2 = 12\left\langle \left[\int_0^t \mathrm{d}s(D_r - \langle D_r \rangle) \right]^2 \right\rangle. \tag{D1}$$

As $t \to 0$, the integral in Eq. (D1) can be approximated as

$$\langle \Delta r^4(t \to 0) \rangle_c = 12t^2\left(\langle D_r^2 \rangle - \langle D_r \rangle^2\right). \tag{D2}$$

The detailed derivation from Eq. (D1) to Eq. (D2) has been provided by Alexandre *et al.* [25]; it aligns with Eq. (D2) in the paper by Chubynsky and Slater [16]. With $\alpha_r(t) = \langle \Delta r^4(t) \rangle_c / \langle \Delta r^2(t) \rangle^2 = [\langle \Delta r^4(t) \rangle / \langle \Delta r^2(t) \rangle^2] - 3$, as $t \to 0$, $\alpha_r(t \to 0)$ can be expressed as the variance of diffusivity, $\mathrm{Var}(D_r)$, divided by the square of the expectation $\langle D_r \rangle^2$:

$$\begin{aligned} \alpha_r(t \to 0) &= \frac{\langle \Delta r^4(t) \rangle_c}{\langle \Delta r^2(t) \rangle^2} = \frac{12t^2\left(\langle D_r^2 \rangle - \langle D_r \rangle^2\right)}{(2\langle D_r \rangle t)^2} \\ &= \frac{3\left(\langle D_r^2 \rangle - \langle D_r \rangle^2\right)}{\langle D_r \rangle^2} = \frac{3\left[E\left(D_r^2\right) - E2(D_r)\right]}{\langle D_r \rangle^2} \\ &= \frac{3\mathrm{Var}(D_r)}{\langle D_r \rangle^2}. \end{aligned} \tag{D3}$$

Equation (D3) provides a way to predict $\alpha_r(t \to 0)$ based on the spatial distribution $p(D_r)$ of D_r. Then, we proceed to derive $\alpha_y(t \to 0)$ for several commonly used spatial distributions $p(D_y)$.

Uniform distribution. Suppose the distribution $p(D_r)$ of D_y follows a uniform distribution, with $D_y \in (D_{\min}, D_{\max}]$, $\beta = D_{\min}/D_{\max}$. In this case, the non-Gaussian parameter can be obtained as

$$3\mathrm{Var}(D_y) = 3\left[\frac{(D_{\max} - D_{\min})^2}{12}\right] = \frac{(D_{\max} - D_{\min})^2}{4}, \tag{D4}$$

$$\langle D_y \rangle = E(D_y) = \frac{D_{\max} + D_{\min}}{2}, \tag{D5}$$

$$\alpha_y(t \to 0) = \frac{3\mathrm{Var}(D_y)}{\langle D_y \rangle^2} = \left(\frac{D_{\max} - D_{\min}}{D_{\max} + D_{\min}}\right)^2 = \left(\frac{1-\beta}{1+\beta}\right)^2. \tag{D6}$$

Standard gamma distribution. As mentioned in the main text, suppose the distribution $p(D_y)$ of D_y follows a gamma distribution and is truncated at $D_y \in [D_{\min}, D_{\max}]$; the detailed derivation for the non-Gaussian parameter is as follows:

$$\begin{aligned} \mathrm{Var}(D_y) &= \mathrm{Var}\left(z\frac{D_{\max} - D_{\min}}{N} + D_{\min}\right) \\ &= \mathrm{Var}(z)\left(\frac{D_{\max} - D_{\min}}{N}\right)^2 \\ &= k\left(\frac{D_{\max} - D_{\min}}{N}\right)^2, \end{aligned} \tag{D7}$$

$$\begin{aligned} \langle D_y \rangle &= \left\langle z\frac{D_{\max} - D_{\min}}{N} + D_{\min} \right\rangle = \langle z \rangle \frac{D_{\max} - D_{\min}}{N} + D_{\min} \\ &= k\frac{D_{\max} - D_{\min}}{N} + D_{\min}, \end{aligned} \tag{D8}$$

$$\begin{aligned} \alpha_y(t \to 0) &= \frac{3\mathrm{Var}(Dy)}{\langle D_y \rangle^2} = 3k\left[\frac{D_{\max} - D_{\min}}{k(D_{\max} - D_{\min}) + ND_{\min}}\right]^2 \\ &= 3k\left[\frac{1-\beta}{k(1-\beta) + N\beta}\right]^2. \end{aligned} \tag{D9}$$

Standard normal distribution. Suppose the distribution $p(D_y)$ of D_y follows a normal distribution truncated at $D_y \in [D_{\min}, D_{\max}]$ during statistical analysis. It can be mapped to a standard normal distribution with a probability density function of $\varphi(z) = (1/\sqrt{2\pi})\exp(-z^2/2)$, with a truncated range of $z \in [-N, N]$. The cumulative distribution function is $\Phi(z) = [1 + \mathrm{erf}(z/\sqrt{2})]/2$, where erf is the error function given by $\mathrm{erf} = (1/\sqrt{\pi})\int_{-z}^{z} \exp(-\tau^2)\mathrm{d}\tau$. For a symmetric truncated range $z \in [-N, N]$, it has $\langle z \rangle \approx 0$, and

$$\begin{aligned} \mathrm{Var}(z|-N \leqslant z \leqslant N) = \sigma^2 \Bigg\{ 1 &- \frac{N\varphi(N) - (-N)\varphi(-N)}{\Phi(N) - \Phi(-N)} \\ &- \left[\frac{\varphi(N) - \varphi(-N)}{\Phi(N) - \Phi(-N)}\right]^2 \Bigg\}. \end{aligned} \tag{D10}$$

Here, $\sigma^2 = 1$, we further obtain

$$\begin{aligned} \mathrm{Var}(z|-N \leqslant z \leqslant N) &= 1 - \frac{N}{\sqrt{2\pi}} \frac{2e - N^2/2}{\Phi(N) - \Phi(-N)} \\ &= 1 - \frac{2\sqrt{2}N}{\sqrt{\pi}} \\ &\quad \times \frac{e - N^2/2}{\mathrm{erf}(N/\sqrt{2}) - \mathrm{erf}(-N/\sqrt{2})}. \end{aligned} \tag{D11}$$

The mapping between D_y and z can be expressed as $D_y = z\frac{D_{\max}-D_{\min}}{2N} + \frac{D_{\max}+D_{\min}}{2}$. Therefore, the non-Gaussian parameter can be obtained by substituting Eqs. (D12) and (D13) into Eq. (D14):

$$\mathrm{Var}(D_y) = \mathrm{Var}\left(z\frac{D_{\max}-D_{\min}}{2N} + \frac{D_{\max}+D_{\min}}{2}\right) = \mathrm{Var}(z|-N\leqslant z\leqslant N)\left(\frac{D_{\max}-D_{\min}}{2N}\right)^2, \quad \text{(D12)}$$

$$\langle D_y\rangle = \left\langle z\frac{D_{\max}-D_{\min}}{2N} + \frac{D_{\max}+D_{\min}}{2}\right\rangle = \langle z\rangle\frac{D_{\max}-D_{\min}}{2N} + \frac{D_{\max}+D_{\min}}{2} + \frac{D_{\max}+D_{\min}}{2}, \quad \text{(D13)}$$

$$\alpha_y(t\to 0) = \frac{3\mathrm{Var}(D_y)}{\langle D_y\rangle^2} = \frac{3}{N2}\left(\frac{D_{\max}-D_{\min}}{D_{\max}+D_{\min}}\right)^2\mathrm{Var}(z|-N\leqslant z\leqslant N) = \frac{3}{N2}\left(\frac{1-\beta}{1+\beta}\right)^2\mathrm{Var}(z|-N\leqslant z\leqslant N). \quad \text{(D14)}$$

For large values of N, such as $N \geqslant 3$, $\mathrm{Var}(z|-N\leqslant z\leqslant N)\approx 1$, resulting in a simplified expression for α_y: $\alpha_y(t\to 0) = \frac{3}{N2}(\frac{1-\beta}{1+\beta})^2$. For small values of N, Eq. (D14) should be used to calculate $\alpha_y(t\to 0)$.

2. Laplace's approximation

The DPD, following Bayes' theorem, $G_s(\Delta y, t) = \int p(D_y)p(\Delta y|D_y)\mathrm{d}D_y$, can be written as

$$G_s(\Delta y, t) = \int_{D_{\min}}^{D_{\max}} \frac{p[D_y(x)]}{\sqrt{4\pi D_y(x)t}}\exp\left[-\frac{\Delta y^2}{4D_y(x)t}\right]\mathrm{d}D_y. \quad \text{(D15)}$$

To handle the integral, we use the Laplace approximation method. This method simplifies the integral expression by approximating the function near its mode peak. We define $f(D_y) = \frac{p[D_y(x)]}{\sqrt{4\pi D_y(x)t}}$ and $g(D_y) = \frac{1}{4D_y(x)t}$, and transform Eq. (D15) into

$$G_s(\Delta y, t) = \int_{D_{\min}}^{D_{\max}} f(D_y)\exp[-\Delta y^2 g(D_y)]\mathrm{d}D_y, \quad \text{(D16)}$$

assuming $D_y(x^*)$ represents the maximum value of $D_y(x)$ at position x^*, where $g(D_y)$ reaches its minimum. This position signifies the most likely location within the probability distribution. Then expanding the Taylor series for $f(D_y)$ and $g(D_y)$ around $D_y(x^*)$ (which will be denoted as D_y^* for convenience), we obtain

$$G_s(\Delta y, t) \approx \int_{D_{\min}}^{D_{\max}} [f(D_y^*) + f'(D_y^*)(D_y - D_y^*)] \times \exp\left(-\Delta y^2\left[g(D_y^*) + g'(D_y^*)(D_y - D_y^*) + \frac{1}{2}g''(D_y^*)(D_y - D_y^*)^2\right]\right)\mathrm{d}D_y. \quad \text{(D17)}$$

Since $g'(D_y^*) = 0$, and keeping the leading term, we obtain

$$G_s(\Delta y, t) \approx f(D_y^*)\exp[-\Delta y^2 g(D_y^*)]\int_{D_{\min}}^{D_{\max}} \times \exp\left[\frac{1}{2}g''(D_y^*)(D_y - D_y^*)^2\right]\mathrm{d}D_y = C\exp\left[-\frac{\Delta y^2}{4D_y^*(x)t}\right]. \quad \text{(D18)}$$

Note that the Laplace approximation assumes that the PDF is unimodal and symmetrical around the mode peak, which might become invalid for complex multimode distributions.

[1] C. Tsallis, S. V. Levy, A. M. Souza, and R. Maynard, Statistical-mechanical foundation of the ubiquity of Levy distributions in Nature, Phys. Rev. Lett. **75**, 3589 (1995).

[2] E. Yamamoto, T. Akimoto, A. Mitsutake, and R. Metzler, Universal relation between instantaneous diffusivity and radius of gyration of proteins in aqueous solution, Phys. Rev. Lett. **126**, 128101 (2021).

[3] A. Sabri, X. Xu, D. Krapf, and M. Weiss, Elucidating the origin of heterogeneous anomalous diffusion in the cytoplasm of mammalian cells, Phys. Rev. Lett. **125**, 058101 (2020).

[4] W. He, H. Song, Y. Su, L. Geng, B. J. Ackerson, H. B. Peng, and P. Tong, Dynamic heterogeneity and non-Gaussian statistics for acetylcholine receptors on live cell membrane, Nat. Commun. **7**, 11701 (2016).

[5] N. Schramma, C. Perugachi Israels, and M. Jalaal, Chloroplasts in plant cells show active glassy behavior under low-light conditions, Proc. Natl. Acad. Sci. USA **120**, e2216497120 (2023).

[6] J. H. Jeon, V. Tejedor, S. Burov, E. Barkai, C. Selhuber-Unkel, K. Berg-Sorensen, L. Oddershede, and R. Metzler, *In vivo* anomalous diffusion and weak ergodicity breaking of lipid granules, Phys. Rev. Lett. **106**, 048103 (2011).

[7] C. Xue, X. Shi, Y. Tian, X. Zheng, and G. Hu, Diffusion of nanoparticles with activated hopping in crowded polymer solutions, Nano Lett. **20**, 3895 (2020).

[8] C. Xue, Y. Huang, X. Zheng, and G. Hu, Hopping behavior mediates the anomalous confined diffusion of nanoparticles in porous hydrogels, J. Phys. Chem. Lett. **13**, 10612 (2022).

[9] Z. Xu, X. Dai, X. Bu, Y. Yang, X. Zhang, X. Man, X. Zhang, M. Doi, and L.-T. Yan, Enhanced heterogeneous diffusion of nanoparticles in semiflexible networks, ACS Nano **15**, 4608 (2021).

[10] M. Hu, H. Chen, H. Wang, S. Burov, E. Barkai, and D. Wang, Triggering Gaussian-to-exponential transition of displacement distribution in polymer nanocomposites via adsorption-induced trapping, ACS Nano **17**, 21708 (2023).

[11] I. Y. Wong, M. L. Gardel, D. R. Reichman, E. R. Weeks, M. T. Valentine, A. R. Bausch, and D. A. Weitz, Anomalous diffusion probes microstructure dynamics of entangled F-actin networks, Phys. Rev. Lett. **92**, 178101 (2004).

[12] C. G. Muresan, Z. G. Sun, V. Yadav, A. P. Tabatabai, L. Lanier, J. H. Kim, T. Kim, and M. P. Murrell, F-actin architecture determines constraints on myosin thick filament motion, Nat. Commun. **13**, 7008 (2022).

[13] F. Rusciano, R. Pastore, and F. Greco, Fickian non-Gaussian diffusion in glass-forming liquids, Phys. Rev. Lett. **128**, 168001 (2022).

[14] B. Wang, S. M. Anthony, S. C. Bae, and S. Granick, Anomalous yet Brownian, Proc. Natl. Acad. Sci. USA **106**, 15160 (2009).

[15] B. Wang, J. Kuo, S. C. Bae, and S. Granick, When Brownian diffusion is not Gaussian, Nat. Mater. **11**, 481 (2012).

[16] M. V. Chubynsky and G. W. Slater, Diffusing diffusivity: A model for anomalous, yet Brownian, diffusion, Phys. Rev. Lett. **113**, 098302 (2014).

[17] A. V. Chechkin, F. Seno, R. Metzler, and I. M. Sokolov, Brownian yet non-Gaussian diffusion: From superstatistics to subordination of diffusing diffusivities, Phys. Rev. X **7**, 021002 (2017).

[18] Y. Lanoiselee, N. Moutal, and D. S. Grebenkov, Diffusion-limited reactions in dynamic heterogeneous media, Nat. Commun. **9**, 4398 (2018).

[19] Y. Lanoiselée and D. S. Grebenkov, A model of non-Gaussian diffusion in heterogeneous media, J. Phys. A **51**, 145602 (2018).

[20] E. Barkai and S. Burov, Packets of diffusing particles exhibit universal exponential tails, Phys. Rev. Lett. **124**, 060603 (2020).

[21] I. Chakraborty and Y. Roichman, Disorder-induced Fickian, yet non-Gaussian diffusion in heterogeneous media, Phys. Rev. Res. **2**, 022020(R) (2020).

[22] J. M. Miotto, S. Pigolotti, A. V. Chechkin, and S. Roldán-Vargas, Length scales in Brownian yet non-Gaussian dynamics, Phys. Rev. X **11**, 031002 (2021).

[23] M. Matse, M. V. Chubynsky, and J. Bechhoefer, Test of the diffusing-diffusivity mechanism using near-wall colloidal dynamics, Phys. Rev. E **96**, 042604 (2017).

[24] R. Pastore, A. Ciarlo, G. Pesce, F. Greco, and A. Sasso, Rapid Fickian yet non-Gaussian diffusion after subdiffusion, Phys. Rev. Lett. **126**, 158003 (2021).

[25] A. Alexandre, M. Lavaud, N. Fares, E. Millan, Y. Louyer, T. Salez, Y. Amarouchene, T. Guerin, and D. S. Dean, Non-Gaussian diffusion near surfaces, Phys. Rev. Lett. **130**, 077101 (2023).

[26] See Supplemental Material at http://link.aps.org/supplemental/10.1103/PhysRevResearch.6.023014 for details as follows: Sec. S1: supplemental experimental methods and measurement uncertainty; Sec. S2: dynamic regulation of diffusivity distribution in simulations; Sec. S3: data of α and β from the literature; Sec. S4: experiment using 500 nm NPs.

[27] H. Xu, X. Zheng, and X. Shi, Surface hydrophilicity-mediated migration of nano/microparticles under temperature gradient in a confined space, J. Colloid Interface Sci. **637**, 489 (2023).

[28] Y. Wen, Z. Li, H. Wang, J. Zheng, J. Tang, P. Y. Lai, X. Xu, and P. Tong, Activity-assisted barrier crossing of self-propelled colloids over parallel microgrooves, Phys. Rev. E **107**, L032601 (2023).

[29] C. Jiang *et al.*, Switch of cell migration modes orchestrated by changes of three-dimensional lamellipodium structure and intracellular diffusion, Nat. Commun. **14**, 5166 (2023).

[30] H. A. Shaban, R. Barth, L. Recoules, and K. Bystricky, Hi-D: Nanoscale mapping of nuclear dynamics in single living cells, Genome Biol. **21**, 95 (2020).

[31] C. Xu, K. Yang, and B. Yuan, Non-Gaussian diffusion of individual lipids unveils the unique peptide-membrane interaction dynamics, J. Phys. Chem. Lett. **14**, 854 (2023).

[32] H. Li, S.-X. Dou, Y.-R. Liu, W. Li, P. Xie, W.-C. Wang, and P.-Y. Wang, Mapping intracellular diffusion distribution using single quantum dot tracking: Compartmentalized diffusion defined by endoplasmic reticulum, J. Am. Chem. Soc. **137**, 436 (2015).

[33] M. Yu *et al.*, Temperature- and rigidity-mediated rapid transport of lipid nanovesicles in hydrogels, Proc. Natl. Acad. Sci. USA **116**, 5362 (2019).

[34] J. Wu, C. Xu, Z. Ye, H. Chen, Y. Wang, K. Yang, and B. Yuan, Transition between different diffusion modes of individual lipids during the membrane-specific action of as-CATH4 peptides, Small **19**, 2301713 (2023).

[35] C. Manzo, J. A. Torreno-Pina, P. Massignan, G. J. Lapeyre Jr., M. Lewenstein, and M. F. G. Parajo, Weak ergodicity breaking of receptor motion in living cells stemming from random diffusivity, Phys. Rev. X **5**, 011021 (2015).

[36] F. Safi Samghabadi, A. H. Slim, M. W. Smith, M. Chabi, and J. C. Conrad, Dynamics of filamentous viruses in polyelectrolyte solutions, Macromolecules **55**, 10694 (2022).

[37] K. A. Rose, N. Gogotsi, J. H. Galarraga, J. A. Burdick, C. B. Murray, D. Lee, and R. J. Composto, Shape anisotropy enhances nanoparticle dynamics in nearly homogeneous hydrogels, Macromolecules **55**, 8514 (2022).

[38] M. J. Skaug, L. Wang, Y. Ding, and D. K. Schwartz, Hindered nanoparticle diffusion and void accessibility in a three-dimensional porous medium, ACS Nano **9**, 2148 (2015).

[39] C. H. Lee, A. J. Crosby, T. Emrick, and R. C. Hayward, Characterization of heterogeneous polyacrylamide hydrogels by tracking of single quantum dots, Macromolecules **47**, 741 (2014).

[40] F. Hofling and T. Franosch, Anomalous transport in the crowded world of biological cells, Rep. Prog. Phys. **76**, 046602 (2013).

[41] M. Baum, F. Erdel, M. Wachsmuth, and K. Rippe, Retrieving the intracellular topology from multi-scale protein mobility mapping in living cells, Nat. Commun. **5**, 4494 (2014).

[42] C. Manzo and M. F. Garcia-Parajo, A review of progress in single particle tracking: From methods to biophysical insights, Rep. Prog. Phys. **78**, 124601 (2015).

[43] L. Xiang, K. Chen, R. Yan, W. Li, and K. Xu, Single-molecule displacement mapping unveils nanoscale heterogeneities in intracellular diffusivity, Nat. Methods **17**, 524 (2020).

[44] T. A. Waigh and N. Korabel, Heterogeneous anomalous transport in cellular and molecular biology, Rep. Prog. Phys. **86**, 126601 (2023).

[45] H. Seckler and R. Metzler, Bayesian deep learning for error estimation in the analysis of anomalous diffusion, Nat. Commun. **13**, 6717 (2022).

[46] D. Ross, M. Gaitan, and L. E. Locascio, Temperature measurement in microfluidic systems using a temperature-dependent fluorescent dye, Anal. Chem. **73**, 4117 (2001).